Check for updates

Small

NANO · MICRO small
www.small-journal.com

RESEARCH ARTICLE

The Rapid Motion of the Leidenfrost Droplet Fired by a Laser

Xin Yan[1] | Hao Wang[1,2] | Lulu Xing[1] | Helong Su[1] | Rui Wu[1] | Jinliang Xu[1,3]

[1]Beijing Key Laboratory of Multiphase Flow and Heat Transfer for Low Grade Energy Utilization, North China Electric Power University, Beijing, P. R. China | [2]CHN Energy New Energy Technology Research Institute Co., Ltd., Beijing, P. R. China | [3]Key Laboratory of Power Station Energy Transfer Conversion and System, Ministry of Education, North China Electric Power University, Beijing, P. R. China

Correspondence: Jinliang Xu (xjl@ncepu.edu.cn)

Received: 13 October 2025 | **Revised:** 11 February 2026 | **Accepted:** 7 May 2026

Keywords: droplet dynamics | leidenfrost droplets | optofluidi | plasmonic bubbles | rapid motion

ABSTRACT

Traditional optofluidic droplet manipulation suffers from low transport efficiency due to the drag of surface tension. This study introduces laser-driven Leidenfrost droplets to achieve rapid, directional transport, with the total acceleration a up to ~60 mm/s^2—approximately triple that of Leidenfrost droplets without a laser. Both higher laser energy and stronger light absorption by the droplet enhance the transport efficiency of Leidenfrost droplets. The kinetic model elucidates that the droplet's rapid motion driven by the laser is attributable to a shift in the droplet's center of mass, induced by the nucleation of plasmonic bubbles. The displacement of the droplet's center of mass generates a driving torque, enhancing droplet internal flow and the vapor film beneath the droplet asymmetry, thereby increasing motion propulsion. This study lays the foundation for efficient light-driven droplet transport, offering valuable insights for advancing the practical application and control of Leidenfrost droplets.

1 | Introduction

Droplet microfluidics is widely applied in various fields, including drug delivery [1], miniaturized chemical reactors [2], micro energy conversion [3], and so on. Utilizing droplets as carriers offers advantages for individual manipulation and efficient mass transfer [4]. However, the practical application of droplet microfluidics faces significant challenges, including limited flexibility and contamination of the carrier during transport. These challenges stem from the contact of the sessile droplet with the substrate [5, 6]. The contact line pinning hinders the droplet motion. Meanwhile, the substrate would contribute to the contamination of the droplet carrier. The Leidenfrost effect, characterized by a vapor layer that levitates droplets above the substrate surface, offers a promising approach to address these challenges [7, 8]. The vapor film beneath the droplet effectively avoids contact line pinning, thereby reducing interfacial friction and minimizing the risk of substrate-induced contamination [9, 10].

When droplets settle on a heated plate, they will exhibit different behaviors, such as gyroscopic rotation [11], floating and drifting [12], and directional movement [13], which are mainly determined by the droplet size and substrate pattern [14]. When Leidenfrost droplets shrink to a suitable dimension (R<1.5 mm), symmetry breaking occurs within the droplets, and the directional motion of the droplet is the main behavior [13, 15]. A singular internal vortex flow is formed in the droplet, which subtly inclines the liquid-gas interface at the droplet's basal region. Thereby, the droplet is self-propelled toward the inclined side [13]. The motion acceleration remains approximately constant and directly relates to the angle of the droplet inclination [16]. Due to the stochastic nature of the vortex flow direction, the droplet's directional motion becomes random,

© 2026 Wiley-VCH GmbH

introducing significant complexity and variability to its transport dynamics.

To achieve fast directional transport, various methods were proposed. Adjusting vapor flow beneath the droplets by altering the macroscopic substrate texture was among the common methods [15, 17]. On Sawtooth surfaces, Leidenfrost droplets actively move toward the steep slopes of the teeth, achieving a peak speed of ~10 cm/s [17, 18]. Via pre-designed textures, Leidenfrost droplets are guided along predetermined paths, which has inspired the design of a novel rotary heat engine [3, 19, 20]. Though effective, this passive method based on surface textures limits dynamic control over droplet trajectories. To enable more flexible directional transport, physical fields like temperature gradients, electric forces, and magnetic forces have been introduced. Temperature gradients on heated substrates create thicker vapor films in hotter regions, propelling droplets toward cooler areas [21–23]. However, substrate thermal inertia significantly limits the flexibility of droplet transport. Electric and magnetic field control methods rely on the conductive solutes (e.g., electrolytes) or magnetic nanoparticles within droplets [24, 25]. While these techniques improve transport flexibility, the mandatory solute inclusion imposes limitations for certain applications.

Light-controlled sessile droplet motion has been widely applied because it can enable remote contactless operation and can be used stably in extremely harsh environments [26, 27]. Within the droplets, photothermal effects create thermocapillary-driven asymmetric flows, directing the droplet to either approach or avoid the heat source [27]. Can laser directional heating also apply to propel the Leidenfrost droplets' motion? For Leidenfrost droplets, the isothermal evaporation interface and the lack of direct contact with the substrate lead to insufficient internal flow and surface friction, hindering effective motion [16, 18]. As a result, achieving and understanding laser-driven motion for Leidenfrost droplets remains a crucial challenge.

This study aims to demonstrate efficient, rapid motion of Leidenfrost droplets via pulsed laser irradiation, while elucidating the mechanisms driving their motion. Variations in single-pulse energy and nanofluid concentration were systematically analyzed to reveal the impact of laser energy and light absorption characteristics on Leidenfrost droplet motion dynamics. Experimental observations and theoretical dynamic modeling revealed that the laser-induced driving force for droplet motion arises from bubble nucleation within the droplets. This process induces a shift in the droplet's centroid and generates torque, which intensifies droplet internal rotational flow, enhances asymmetry in the bottom vapor film, and increases the tilt angle of the droplet's base interface. The horizontal component of gravity propels the droplet motion. Compared to traditional light-controlled transport methods, this study introduces an ingenious method for rapid directional droplet motion on solid surfaces. Alternatively, the enhanced internal rotational flow in droplets under laser irradiation offers potential applications in micro–energy harvesting, microfluidics, microreactors, and biomedical systems.

2 | Results and Discussion

2.1 | Leidenfrost Droplets Fast Motion Fired by a Laser

The 527 nm pulsed laser was used to irradiate the Leidenfrost droplet. Due to the weak absorption of the deionized water at 527 nm, a small amount of gold nanoparticles (AuNPs) was added into the droplet to enhance the light absorption. The gold nanofluid was prepared via the citrate reduction method (as detailed seen in Section 4.2). A gold nanofluid droplet was placed on a hot substrate, exhibiting the Leidenfrost effect, as shown in Figure 1a. A laser irradiates the droplet from the left. When droplets are placed on the bar, the droplets levitate beneath the needle briefly, then rapidly move right just like bullets fired along the orbit (see Movie S1). At a fixed $E_l = 6$ mJ, the average speed of the droplets increases with the nanofluid concentration, as shown in Figure 1b. For a fixed displacement ($\Delta x = 35$ mm), droplets with higher c_i or higher E_l consistently reach the endpoint faster (Figure 1c), demonstrating a strong correlation between motion velocity, nanofluid concentration, and laser pulse energy. Travel time for droplets with high c_i decreases linearly as E_l increases. However, the droplets of c_i = 100 ppm show an anomalously constant travel time regardless of E_l, suggesting that while absorbed laser energy directly affects motion speed, additional factors also influence droplet dynamics.

The droplet center trajectories were analyzed and found to fit well with parabolic curves (Figure 2a). By differentiating the fitted curves, the actual acceleration a of Leidenfrost droplets, defined as $a = d^2x/dt^2$, was obtained, with typical values ranging between 18.5 and 58.5 mm/s^2. Achieving an ideal level of substrate is practically challenging. Even a slight inclination can significantly affect droplet acceleration. In the experiments, the horizontal tilt angle α_s was controlled to within 0.1 mrad, corresponding to an induced acceleration of approximately 1.0 mm/s^2, which is negligible compared to the observed droplet accelerations a and thus disregarded. However, even on a perfectly level surface, millimeter-scale Leidenfrost droplets inherently exhibit spontaneous accelerated motion due to symmetry-breaking of internal flows [13]. The direction of this acceleration is observed to be random, occurring either to the right or to the left on the bar. However, for the Leidenfrost droplet subjected to laser irradiation, the droplets levitate and remain beneath the needle briefly, as shown in the insert figure of Figure 2a. In this period, the asymmetrical laser irradiation triggers a symmetry-breaking of internal flow in the droplet. Whether the Marangoni force F_{ma} or the buoyancy lift force F_b caused by laser heating, which will be discussed later, they both tend to generate a clockwise internal flow in the Leidenfrost droplet. Thus, the direction of internal flows is certain during the droplet levitation beneath the needle after detaching from it. And the rightward is adopted for the acceleration arising from symmetry-breaking of internal flows. Control experiments on Leidenfrost droplets without laser irradiation established a baseline acceleration of ~18 mm/s^2 (red curve in Figure 2a), consistent with previous reports [13]. For clarity, the total acceleration a of laser-driven Leidenfrost droplets is decomposed into a_0 and a_l. a_0 is the baseline acceleration (18 mm/s^2) due to symmetry-breaking of

16136829, 0, Downloaded from https://onlinelibrary.wiley.com/doi/10.1002/smll.202512574 by Jinliang Xu - North China Electric Power University Beijing , Wiley Online Library on [12/05/2026]. See the Terms and Conditions (https://onlinelibrary.wiley.com/terms-and-conditions) on Wiley Online Library for rules of use; OA articles are governed by the applicable Creative Commons License

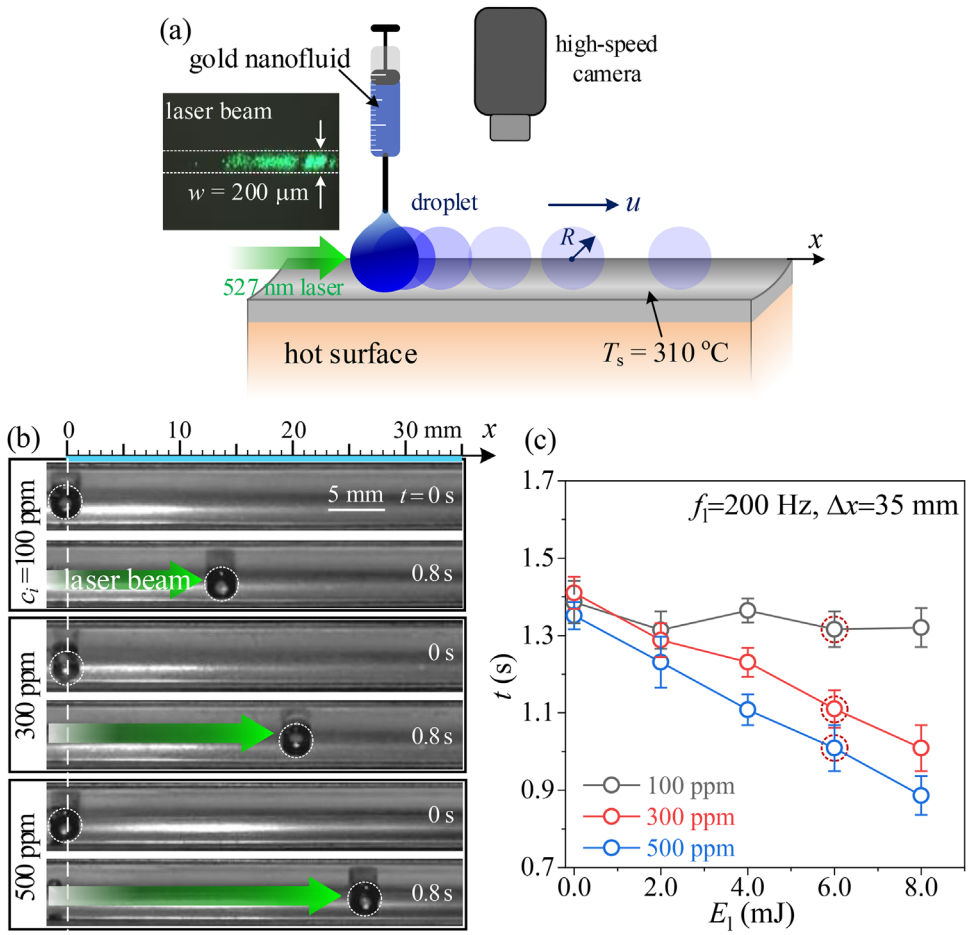


FIGURE 1 | Behavior of Leidenfrost droplets under laser propulsion. (a) Schematic of the experiment: a quasi-spherical nanofluid droplet with radius R sits on a brass bar with a temperature of 310°C. The surface of the brass bar is slightly curved in the direction perpendicular to the x-axis. A pulse laser of 527 nm irradiates the center of the Leidenfrost droplet from left. Inset: the visualization of the laser beam. (b) Top-view chronophotograph showing laser-propelled droplets with radius $R = 1.25$ mm. The single pulse energy of the laser is 6 mJ. The droplets initiate at $x_0 = 0$ mm on a bar heated to 310°C. The droplet travel distance within the same duration increases with the nanofluid concentration. (c) Influence of single pulse energy and nanofluid concentration on the arrival time of droplets traveling a distance of 35 mm.

internal flows in droplets, and a_l is the laser-induced acceleration. The following discussion focuses on the mechanisms behind a_l.

The dependence of laser-induced acceleration a_l on nanofluid concentration c_i and single-pulse laser energy E_l is summarized in Figure 2b, with error bars representing standard errors from five independent measurements. The results demonstrate that laser-induced acceleration a_l increases with both E_l and c_i, reaching a maximum of approximately 40 mm/s^2, roughly double the baseline acceleration a_0. This indicates that the laser-induced driving force is comparable in magnitude to the self-propulsion force F_p arising from symmetry breaking, highlighting the significant role of laser irradiation. Notably, the sensitivity of a_l to E_l shows a marked dependence on c_i. For droplets with low c_i, the acceleration response is subdued, reaching only about 3 mm/s^2 even at higher E_l, indicating a weak coupling between absorbed light energy and propulsion. Conversely, for high c_i droplets, a_l increases almost exponentially with E_l, suggesting a much stronger coupling effect. The relation between a_l and c_i is nonlinear, which emphasizes the intricate interplay between c_i and E_l in driving droplet motion. The acceleration is not a simple linear function of laser power, but rather involves a highly coupled mechanism, likely driven by enhanced photothermal conversion and localized vapor dynamics. The mechanisms responsible for the pronounced concentration-dependent acceleration a_l will also be elucidated.

2.2 | Propelling Mechanism of the Leidenfrost Droplets Fired by a Laser

Apart from the self-propulsion force $F_p = ma_0$, originating from symmetry-breaking of internal flows within the droplets, several additional forces may contribute to the motion of laser-driven Leidenfrost droplets. These include the Marangoni force F_{ma}, buoyancy lift force F_b, indirect light force F_i, and nucleated bubble induced buoyancy force F_n, as illustrated in Figure 3. The self-propulsion force F_p is predominantly induced by the symmetry-breaking internal flows and is characterized by a characteristic fluid velocity U_0 [13].

$$F_p \sim \frac{\rho_l g \mu_v R^7 U_0}{\sigma(\delta l_c)^2} \quad (1)$$

16136829, 0, Downloaded from https://onlinelibrary.wiley.com/doi/10.1002/smll.202512574 by Jinliang Xu - North China Electric Power University Beijing , Wiley Online Library on [12/05/2026]. See the Terms and Conditions (https://onlinelibrary.wiley.com/terms-and-conditions) on Wiley Online Library for rules of use; OA articles are governed by the applicable Creative Commons License

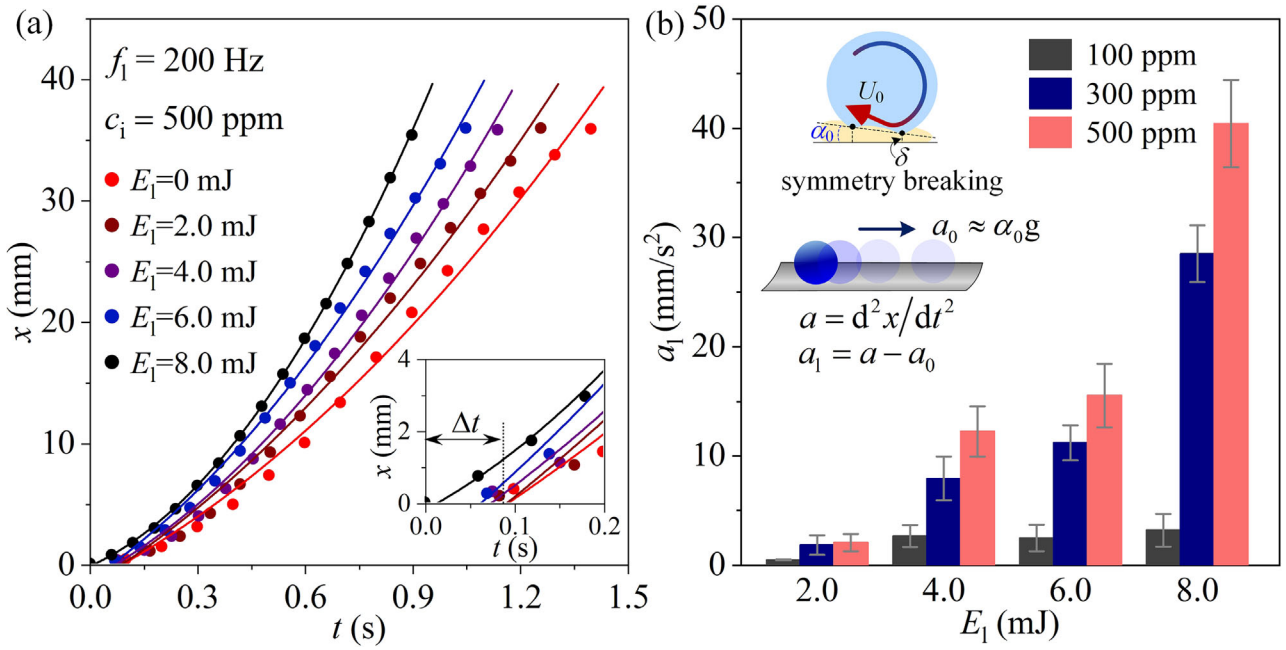


FIGURE 2 | Dynamics of laser-propelled Leidenfrost droplets: (a) Position x of the droplet as a function of time t. Each curve is fitted by a quadratic function (drawn with a solid line), from which we deduce the absolute acceleration a. The inserted figure is the enlarged view of the droplets' position at the initial time. (b) The laser-propelled acceleration a_l as a function of the nanofluids concentration $c_{i,}$ and pulse energy E_l. The error bars show the standard dispersion of the data. Inset: the symmetry-breaking induced acceleration a_0 of Leidenfrost droplets on a flat surface without laser irradiation.

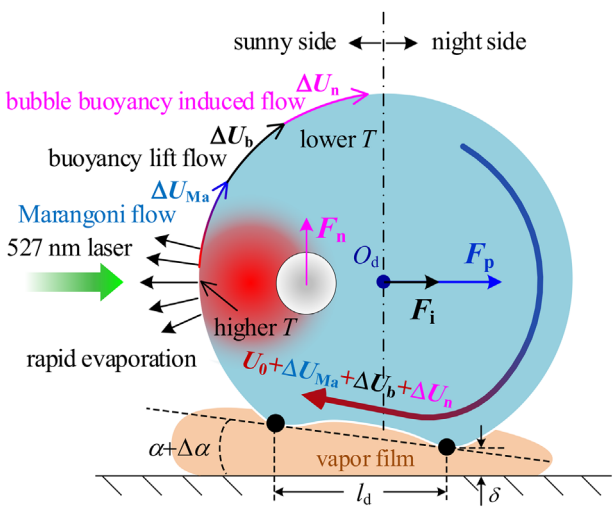


FIGURE 3 | Forces that may act on the light-propelled Leidenfrost droplet. The symmetry breaking of flow within a Leidenfrost droplet induces a driving force F_p. Rapid evaporation at the laser incident point generates propelling forces F_i. Additionally, the surface temperature at the laser incident point is higher than that at the apex of the droplet. This temperature gradient gives rise to the Marangoni flow ΔU_{Ma} and buoyancy-driven lift flow ΔU_b. The nucleated bubble in the droplet will move upward, inducing the clockwise flow ΔU_n. As the flow speed increases, it further enhances the symmetry breaking of the droplet's internal flow, thereby amplifying the driving forces.

where ρ_l denotes the density of the nanofluid, μ_v represents the dynamic viscosity of the vapor, R is the droplet radius, σ refers to the surface tension coefficient of the nanofluid, and l_c is the capillary length of the nanofluid, $l_c = \sqrt{\sigma/(\rho_l g)}$. δ represents the characteristic thickness of the vapor film beneath the droplet, which can be determined using the following expression for $R<l_c$ [28].

$$\delta \sim \left(\frac{\lambda_v \Delta T_{sat} \rho_l \mu_v g}{h_{fg} \rho_v \sigma^2}\right)^{1/3} R^{4/3} \quad (2)$$

where λ_v represents the thermal conductivity of the vapor layer, ΔT_{sat} denotes the temperature difference between the substrate temperature T_s and the liquid's saturation temperature T_{sat}, ρ_v is the density of the vapor, and h_{fg} is the latent heat of vaporization. Based on the baseline experimental data presented in Figure 2a, the self-propulsion force can be estimated as $F_p \approx ma_0 = 1.47 \times 10^{-7}$ N. Correspondingly, the internal flow velocity U is approximately 40 mm/s. This is useful to analyze the effect of the Marangoni force F_{ma}, the buoyancy lift force F_b, and the nucleated bubble-induced buoyancy force F_n on Leidenfrost droplet motion.

The Marangoni force F_{ma} originates from surface tension gradients induced by non-uniform temperature distributions on the droplet surface during laser heating. This force drives internal fluid motion, raising the characteristic internal flow velocity to $U_0+\Delta U_{ma}$ within the droplet, thereby intensifying the symmetry-breaking effect and amplifying the self-propulsion force (as illustrated in Figure 3). Infrared camera measurements of the droplet surface temperature evolution (refer to Figure S1) indicate a temperature difference $\Delta T \sim 1.0°C$ between the laser irradiation point and the droplet apex. This temperature gradient generates a Marangoni-induced flow $\Delta U_{ma} \sim (|d\sigma/dT|\Delta T/\rho R)^{1/2} \approx 7$ mm/s, which is an order of magnitude smaller than the characteristic internal velocity $U_0 \sim$ 40 mm/s, demonstrating that the propulsion

16136829, 0, Downloaded from https://onlinelibrary.wiley.com/doi/10.1002/smll.202512574 by Jinliang Xu - North China Electric Power University Beijing , Wiley Online Library on [12/05/2026]. See the Terms and Conditions (https://onlinelibrary.wiley.com/terms-and-conditions) on Wiley Online Library for rules of use; OA articles are governed by the applicable Creative Commons License

effect resulting from Marangoni flow is substantially weaker than the self-propulsion force F_p.

Laser heating generates a localized hot spot, resulting in a buoyancy force F_b that induces upward fluid motion within the droplet, further increasing the internal flow velocity to $U_0+\Delta U_b$ (as depicted in Figure 3). For water, the thermal expansion coefficient β is approximately 0.7×10^{-4} K^{-1}. Assuming a balance between the buoyancy force and viscous resistance, $\rho_l g\beta\Delta TR^3 \approx \rho\Delta U_b{}^2R^2$, the characteristic velocity increment ΔU_b is estimated as $(g\beta\Delta TR)^{1/2} \approx 4.2$ mm/s. This value is an order of magnitude smaller than the typical internal flow speed $U_0 \sim 40$ mm/s, indicating that the propulsion effect attributed to buoyancy is negligible. However, the internal flow induced by the Marangoni force F_{ma} and buoyancy force F_b can be the trigger of the symmetry breaking of internal flow.

Indirect light pressure arises from the asymmetric laser illumination of the droplet [29]. When the laser irradiates the droplet from one side, it creates a sunny side and a night side (as illustrated in Figure 3). On the sunny side, the liquid absorbs more laser energy, leading to increased local evaporation rates, while the night side absorbs less energy, resulting in reduced evaporation. This disparity in vapor generation rates across the droplet's gas-liquid interface induces a vapor momentum imbalance, producing a force that propels the droplet away from the laser source, which can be determined by

$$F_i \sim \frac{\pi}{\rho_v}\left(\frac{\Delta q r_1}{h_{fg}}\right)^2 \tag{3}$$

where r_l denotes the radius of the laser beam, and Δq represents the laser heat flux difference between the sunny and night sides of the droplet. The heat flux differential depends on laser parameters, nanofluid concentration, and the photothermal conversion efficiency of the nanofluid. In the experiments, the $\Delta q \approx 10^5 f_l E_l$, yielding $F_i \approx 10^{-10}$ N. This is three orders of magnitude smaller than the self-propulsion force F_p, thereby indicating that the contribution of indirect light pressure to droplet propulsion is negligible.

These analyses demonstrate that the previously considered forces, Marangoni force F_{ma}, buoyancy lift force F_b, and indirect light force F_i, are substantially weaker than the laser-induced acceleration force ma_l observed in experiments. This suggests the existence of other, more dominant mechanisms driving the rapid motion of laser-driven Leidenfrost droplets. Further investigation of laser-irradiated Leidenfrost droplets reveals the presence of bubbles within the droplets (refer to Figure 4a). These bubbles, termed plasmonic bubbles, arise from the absorption of laser energy and subsequent photothermal conversion facilitated by the nanofluid [30]. We hypothesize that the presence of these bubbles significantly influences the internal flow dynamics of the droplet, potentially altering the characteristics of the vapor film beneath it, as shown in Figure 3. Consequently, the overall motion dynamic behavior of the droplet is modified. To validate this hypothesis, a detailed analysis of bubble dynamics within the droplets is conducted.

The nucleation, movement, and collapse dynamics of bubbles within droplets are illustrated in Figure 4a. Unlike the conventional understanding, where bubbles typically rupture through the droplet's apex liquid-gas interface, this study reveals a closed 'nucleation-rise-collapse' cycle occurring entirely within the droplet, coupled with the internal fluid motion. In this process, nanofluid droplets absorb laser energy, resulting in localized superheating and subsequent bubble nucleation. The nucleated bubbles rise swiftly due to the buoyant force F_n, following a clockwise trajectory, and eventually condense and collapse. The typical cycle duration for bubbles is approximately 10 ms. This self-contained bubble dynamics behavior is observed across a wide range of laser single pulse energies E_l, and nanofluid concentrations c_i. The location of nucleation sites and the size of the bubbles strongly depend on both E_l and c_i. With higher E_l, the bubble size correspondingly grows, which can be attributed to the increased energy input, shown as Figure 5b. Additionally, an increase in c_i causes the nucleation site to shift closer to the laser incidence point. The nucleation site is influenced by the optical absorption characteristics of the nanofluid and the internal heat dissipation mechanisms. For droplets with high c_i, superior photothermal conversion efficiency minimizes the effects of heat dissipation, causing the superheated region and nucleation site to be closer to the laser incidence point. Conversely, in droplets with lower c_i, the absorbed laser energy is relatively modest, leading to bubble nucleation nearer to the droplet center, where the heat dissipation path is longer. The horizontal distance x_b between the plasmonic bubble's center and the droplet's center (see Figure 4a) quantifies bubble position. The distance $x_{b,s}$ measure in images was corrected to the true distance x_b. The variation of x_b for droplets with varying c_i at $E_l = 8$ mJ is presented in Figure 4b. And the variation of $x_{b,max}$ for different c_i and E_l is shown in Figure 4c. The results show that x_b increases significantly as c_i rises, illustrating the strong influence of nanofluid concentration on bubble dynamics. Here, the bubble offset x_b is defined within a two-dimensional plane, which is the plane that passes through the center of the droplet and is parallel to the horizontal plane of the image. In reality, bubble motion is inherently three-dimensional, and any out-of-plane displacement may induce droplet motion perpendicular to the image plane. Nevertheless, the slight curvature of the bottom track enables the droplet to self-correct and remain confined to the track. Moreover, because the motion can be decomposed into components, the in-plane bubble displacement directly corresponds to lateral droplet motion. Consequently, restricting the analysis of bubble offset to two-dimensional motion does not compromise the subsequent analysis.

The formation of bubbles shifts the droplet's mass center O_m relative to its geometric center O_d, producing a sustained driving torque that induces an increment of clockwise rotational speed $\Delta\Omega$ (as shown in Figure 5a). Characterizing the internal flow field of the droplet using the PIV method is challenging due to the droplet's rapid motion. The tracer particles cannot be reliably tracked and analyzed by the software under these conditions. Nevertheless, theoretical analysis indicates the presence of an internal clockwise rotation within the droplet. First, previous studies have confirmed that symmetry breaking can induce such clockwise rotation, thereby generating a self-propulsion force [13]. Second, the upward motion of bubbles entrains the

16136829, 0, Downloaded from https://onlinelibrary.wiley.com/doi/10.1002/smll.202512574 by Jinliang Xu - North China Electric Power University Beijing , Wiley Online Library on [12/05/2026]. See the Terms and Conditions (https://onlinelibrary.wiley.com/terms-and-conditions) on Wiley Online Library for rules of use; OA articles are governed by the applicable Creative Commons License

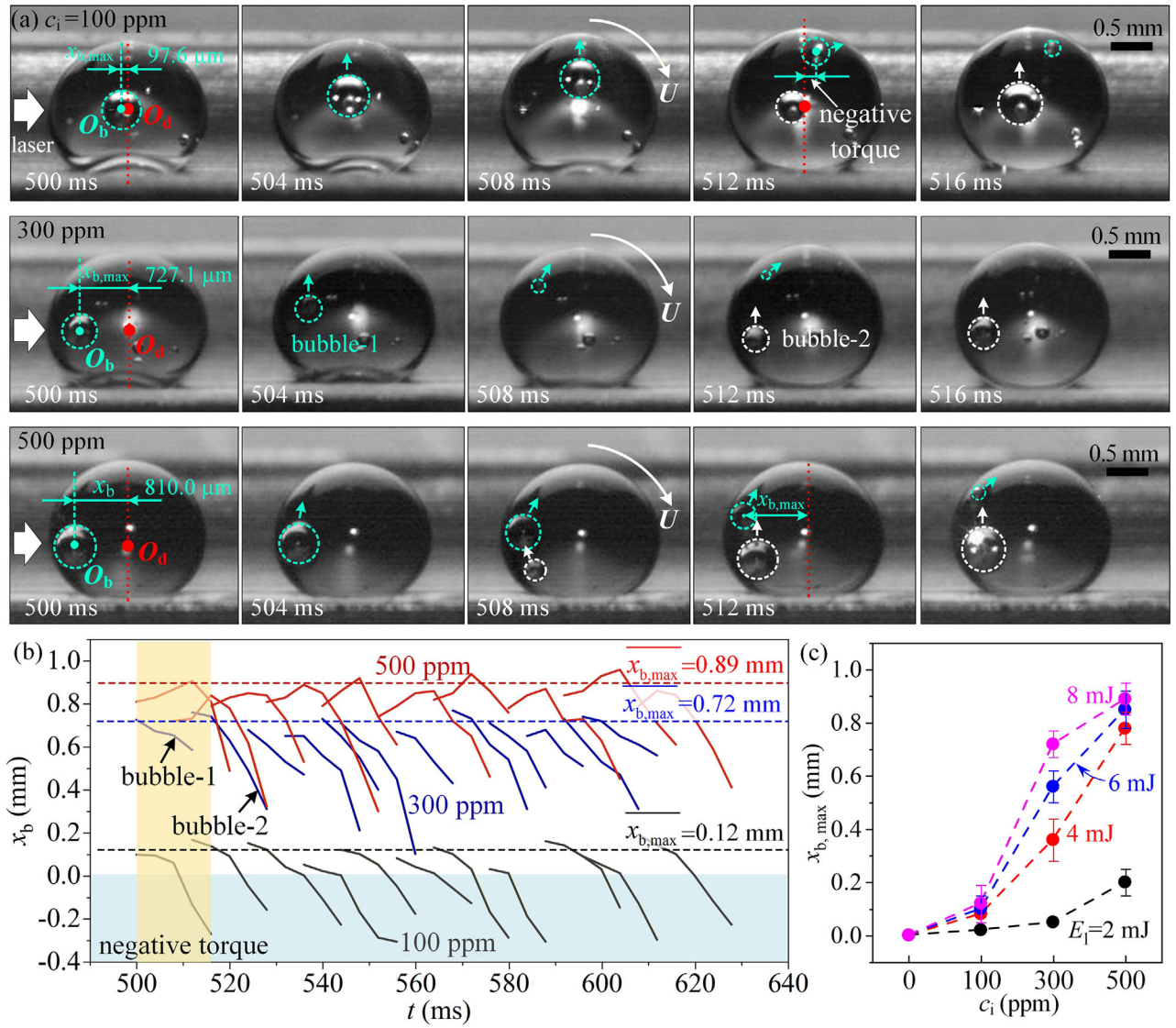


FIGURE 4 | Chronophotograph showing light-propelled droplets with an encapsulated bubble. (a) The encapsulated bubble is generated at varying locations within the droplet depending on the nanofluid concentration. The single pulse energy of the incident laser is 8 mJ. Bars show a spatial scale of 0.5 mm. The distance between the bubble center $O_{b,}$ and the droplet center O_d denoted as x_b. The x_b is the true value corrected from the image-measured value $x_{b,s}$. The curved light–shadow patterns observed at the bottom of the droplet in the subgraph (a) are not caused by a tilt of the vapor layer beneath the droplet. Instead, it originates from the reflection of the curved substrate surface within the droplet during its vertical oscillation along the substrate, which can be clearly observed in Movie S2. Under the present experimental conditions, any tilt of the vapor layer beneath the droplet is not readily observable. (b) The variation of x_b over time for droplets of different nanofluid concentrations. The $\overline{x_{b,max}}$ is defined as the average value of the maximum distance between the center of the bubble and the droplet center for different bubbles. The time period depicted in subgraph (a) corresponds to the yellow shaded area of subgraph (b). The blue shaded area indicates that the torques produced by the bubbles are negative, which hinder the clockwise rotation of the droplet. (c) The maximum horizontal displacement of the bubble center.

surrounding liquid, which further contributes to the formation of clockwise rotation. The clockwise rotation of the bubble enhances the internal circulation within the droplet, which consequently increases the tilt angle of the droplet's bottom interface and generates an additional laser-induced force. The mechanism underlying this laser-induced force is fully consistent with the self-propulsion induced by symmetry breaking [13]. Therefore, the scaling-laws established in previous works can be directly applied in the present analysis. Building upon these foundations, the additional laser-induced flow velocity should be derived, from which the corresponding laser-induced force can be determined. The theoretical framework employed here follows the scaling-law approach, where both sides of each derived equation remain of the same order of magnitude. This consistency enables direct comparison between experimental measurements and theoretical predictions, thereby validating the observed trends. Despite the continuous movement of bubbles within the droplet, their periodic nucleation sustains the driving torque, as depicted in Figure 4. This torque depends on the droplet's mass and the offset distance x_m of O_m. The torque induced by the offset of the mass center forms a force couple with the torque generated by the buoyant force of the bubble, i.e., $_m = mgx_m \approx \rho_1 g r_b^3 x_b$(detail provided in the Supplementary Information). The laser-driven torque Π_m is balanced by the resistive torque Π_d arising from

16136829, 0, Downloaded from https://onlinelibrary.wiley.com/doi/10.1002/smll.202512574 by Jinliang Xu - North China Electric Power University Beijing , Wiley Online Library on [12/05/2026]. See the Terms and Conditions (https://onlinelibrary.wiley.com/terms-and-conditions) on Wiley Online Library for rules of use; OA articles are governed by the applicable Creative Commons License

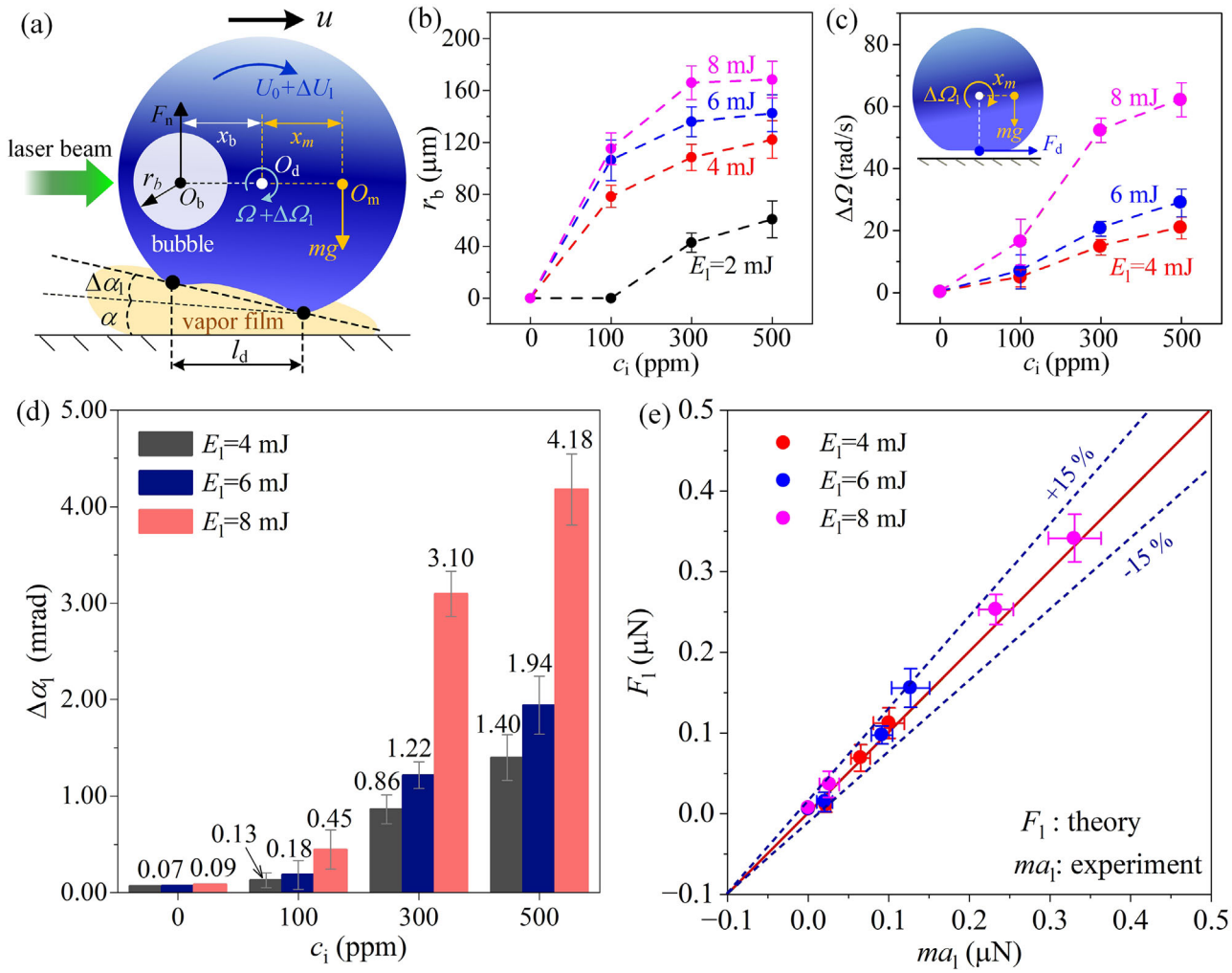


FIGURE 5 | The model of laser-propelled Leidenfrost droplet: (a) Two-dimensional model of Leidenfrost droplets with an encapsulated plasmonic bubble; (b) The radius of the bubble in the droplet for different single pulse energy and concentration; (c) Enhanced rolling rotation of Leidenfrost droplets irradiated by light. The inset is the balance between the driving torque resulting from the shift in droplets centroid and resisting moment arising from vapor film dissipation beneath the droplet; (d) The tilt angle increment $\Delta\alpha_\lambda$ induced by laser irradiation in relation to the c_i and E_l; (e) The comparison of the laser-propelled force between the measured value ma_l and the model-calculated value F_l. The solid line shows the $ma_l = F_l$, and error bars correspond to the standard deviation along both the *x*-axis and the *y*-axis.

the viscous dissipation within the vapor film beneath the droplet. The Π_d can be estimated using $\Pi_d = F_d \cdot R \sim \mu_v \Omega R^6/\delta l_c^2$ [31]. Thus, the change of clockwise rotational speed $\Delta\Omega$ is given by

$$\Delta\Omega \sim \frac{\rho_l g r_b^3 l_c^2 \delta x_b}{\mu_v R^6} \tag{4}$$

This enhances the internal fluid flow velocity $\Delta U = \Delta\Omega R$, amplifying the symmetry breaking of fluid motion within the droplet. The horizontal displacement of the bubble center x_b varies continuously over time. For simplicity, the average value of maximum $\overline{x_{b,max}}$ for different bubbles, shown in Figure 4b, is taken as the x_b in Equation (4), and the result is presented in Figure 4c. Substituting experimental data, it is observed that within the concentration range of 100–500 ppm, the laser-induced torque increases from 0.16×10^{-12} to 1.46×10^{-12} N·m at $E_l = 8.0$ mJ. This raises the droplet's rotational speed by 16–62 rad/s, tilting the droplet's bottom interface by 0.5–4.2 mrad (Figure 5c,d). A similar trend is also observed for $E_l = 4.0$ and 6.0 mJ. This induces an additional horizontal gravitational component $mg\Delta\alpha_l$, which serves as the light-driven force F_l for the rapid motion of the laser-irradiated Leidenfrost droplet. Based on Equations (1) and (4), the driving force F_l is expressed as:

$$F_l \sim \frac{\rho_l g \mu_v R^7 \Delta U}{\sigma \delta^2 l_c^2} = \frac{\rho_l g \mu_v R^7}{\sigma \delta^2 l_c^2} \times \frac{\rho_l g r_b^3 l_c^2 \delta x_b R}{\mu_v R^6} = \frac{\rho_l^2 g^2 r_b^3 x_b R^2}{\sigma \delta} \tag{5}$$

where ρ_l denotes the density of the nanofluid, μ_v represents the dynamic viscosity of the vapor, R is the droplet radius, σ refers to the surface tension coefficient of the nanofluid, and l_c is the capillary length of the nanofluid, $l_c = \sqrt{\sigma/(\rho_l g)}$. δ represents the characteristic thickness of the vapor film beneath the droplet, which can be obtained by Equation (2).

Figure 5e compares the driving force F_l calculated using Equation (5), with the experimental values ma_l derived from the motion curves of droplets at various c_i and E_l. The two sets of data

16136829, 0, Downloaded from https://onlinelibrary.wiley.com/doi/10.1002/smll.202512574 by Jinliang Xu - North China Electric Power University Beijing , Wiley Online Library on [12/05/2026]. See the Terms and Conditions (https://onlinelibrary.wiley.com/terms-and-conditions) on Wiley Online Library for rules of use; OA articles are governed by the applicable Creative Commons License

exhibit excellent correspondence, with deviations within ± 15%. This validates that the laser-induced driving force in irradiated Leidenfrost droplets arises from the asymmetric distribution of plasmonic bubbles. Such asymmetry accelerates internal flow, increasing the tilt angle $\Delta\alpha_l$ at the droplet base, thereby generating an additional horizontal gravitational component that propels the droplet. The overall motion of droplets detached from the needle can be described as follows: asymmetrical laser irradiation induces symmetry breaking of the internal flow within the droplets and liquid-gas interface incline beneath the droplet; during their subsequent motion, plasmonic bubble nucleation further enhances their propulsion (as shown in Movie S2).

An unresolved aspect is the insensitivity of droplet acceleration a_l to E_l at low c_i. The light-driven force F_l depends on both the plasmonic bubble radius r_b and the offset distance x_b. At low c_i, plasmonic bubble nucleation predominantly occurs near the droplet center, with increased E_l primarily enlarging r_b but minimally affecting x_b. While Equation (5) predicts an increase in F_l with larger r_b, the upward motion of bubbles tends to shift them leftward into the droplet's right hemisphere (the blue shaded area in Figure 4b), generating a counterclockwise torque that partially counteracts the clockwise internal flow. This mitigates the effect of bubble size increase, rendering a_l insensitive to E_l. Conversely, at high c_i, bubble nucleation occurs closer to the droplet interface. Higher E_l significantly enlarges both r_b and x_b, leading to an exponential rise in a_l with increasing E_l. For droplets with concentrations of $c_i = 300$ and 500 ppm, the incident laser energy is nearly fully absorbed due to the sufficiently high concentration, leading to minor differences in the size of the nucleated bubbles. However, compared with the 300 ppm case, bubbles generated in 500 ppm droplets are located closer to the droplet edge, thereby producing a larger torque. Overall, as the nanofluid concentration increases from 100 to 300 ppm, the laser-induced acceleration a_l increases markedly. In contrast, further increasing the concentration from 300 to 500 ppm results in a much more gradual enhancement.

2.3 | Comments

The increase in internal rotation flow velocity of the droplet due to plasmonic bubbles under laser irradiation is consistent across different nanofluids and laser wavelengths, as long as the nanofluid has strong laser absorption. Figure S2a illustrates the motion dynamics of different nanofluid droplets under varying laser wavelengths. The gold nanofluid (AuNF) droplet irradiated with a 527 nm laser exhibits a higher velocity than one irradiated with a 405 nm laser. As shown in Figure S2b, the absorption peak of AuNF is around 525 nm, near 527 nm, resulting in greater light absorption at 527 nm compared to 405 nm. For the same nanofluid concentration, the 527 nm laser irradiation generates more heat, leading to a larger plasmonic bubble radius r_b and offset distance x_b to have high rotational speed $\Delta\Omega$ and internal fluid flow velocity ΔU. The silver nanofluid (AgNF) droplets show opposite motion characteristics, as their absorption peak occurs at 407 nm. Meanwhile, Carbon nanotube nanofluid (CNT-NF) droplets achieve high motion acceleration under both 405 and 527 nm irradiation, reflecting their broad and efficient absorption properties, as illustrated in Figure S2b. Therefore, the driving force of laser irradiation originates from the photo-thermal effect of the nanofluid, and it can be applied to other working fluids as well.

This study is focused on discovering the mechanism of the fast motion of laser-induced Leidenfrost droplets. The rapid motion of the droplet arises from laser-enhanced symmetry breaking within its interior. This symmetry breaking is observed only when the droplet radius lies between approximately 0.7 and 1.5 mm [13]. For larger droplets ($R > 1.5$ mm), the two internal convective flows inside the droplet cannot sufficiently tilt the droplet's bottom interface, and thus fail to generate a self-propulsion force. Conversely, for smaller droplets ($R < 0.7$ mm), the internal flow strength is reduced due to viscous resistance, which also leads to weaker self-propulsion. Limited by the experimental conditions, the experiments were performed only on a straight brass bar. Nevertheless, it is reasonable to anticipate that Leidenfrost droplets could exhibit more complex motions along intricate trajectories by switching the direction of laser irradiation. However, due to the inertial effects of the internal flow within the droplet and the rapid droplet motion, the laser-guided following behavior may not be ideal at present and warrants further investigation in future work.

Furthermore, the plasmonic bubble–driven rotational enhancement in Leidenfrost droplets would offer applications in micro–energy harvesting, microfluidics, microreactors, and biomedicine. For micro–energy harvesting, rotation in charged droplets enables charge separation to generate potential difference and current, serving as miniature optical-to-electrical converters [32, 33]. The contactless nature reduces frictional energy dissipation. This study provides a new insight into regulating the rotational speed of the droplet heat engine by adjusting the direction and intensity of laser irradiation. In microfluidics and microreactors, rotational flow enhances convective mixing, overcoming diffusion-limited transport and enabling rapid, uniform reactions—useful for material synthesis and biosensing [34, 35]. In biomedical contexts, this mechanism accelerates reactions in samples such as cells, DNA, and proteins, improving drug screening and pathogen detection [36, 37]. In such applications, safety-related temperature thresholds are crucial. Typically, cells and proteins remain stable within the range of approximately 33°C to 37°C, whereas DNA amplification via PCR operates between about 70°C and 98°C [38, 39]. In the present study, measuring the internal temperature of moving droplets is highly challenging due to their small size and rapid motion. The temperature around the bubble within the droplet is close to the boiling point (approximately 100°C for water) but decreases sharply away from the bubble, which accounts for the observed reduction in bubble size during upward motion. The surface temperature of the droplet was measured from the top view using an infrared imager (see Figure S1). The maximum measured surface temperature of the droplet is below 96°C, which is suitable for PCR-based DNA amplification but not suitable for cells or proteins. Nevertheless, utilizing low–boiling-point working fluids—such as alcohols or other organic liquids—or operating in a reduced-pressure environment could allow precise regulation of droplet temperature within biologically acceptable limits. The droplets themselves have unique physicochemical properties, which require further exploration and practical implementation.

16136829, 0, Downloaded from https://onlinelibrary.wiley.com/doi/10.1002/smll.202512574 by Jinliang Xu - North China Electric Power University Beijing , Wiley Online Library on [12/05/2026]. See the Terms and Conditions (https://onlinelibrary.wiley.com/terms-and-conditions) on Wiley Online Library for rules of use; OA articles are governed by the applicable Creative Commons License

3 | Conclusions

This study investigates the kinetic behavior of Leidenfrost droplets irradiated by a laser, which exhibits rapid, bullet-like directional motion. The droplets' acceleration depends on both the laser power and their light absorption capability. An increase in laser power, coupled with enhanced light absorption properties, significantly amplifies the motion of the Leidenfrost droplets. The droplet acceleration reaches up to 40 mm/s^2—double the acceleration observed without laser irradiation.

A dynamic model was developed to characterize laser-driven Leidenfrost droplet motion. The calculated light-driven force F_l closely matches experimental data, demonstrating that F_l originates from the asymmetric distribution of plasmonic bubbles within the droplets. This asymmetry intensifies symmetry-breaking of the internal flow and increases the inclination angle of the droplet's base, thereby producing a horizontal component of its weight that propels the droplet's forward motion. For droplets with weaker light absorption capacities, acceleration a_l exhibits insensitivity to variations in pulse energy E_l. This is attributed to the plasmonic bubbles predominantly nucleating near the center of the droplet. During their rise, bubbles exert counterclockwise torque that hinders clockwise internal flow, thus limiting a_l despite increasing E_l.

This study lays a foundation for remote, non-intrusive, and droplet-directional fast transport technologies. The established dynamics model for light-driven Leidenfrost droplets will aid in enhancing their practical applications and further development.

4 | Experiment and Materials

4.1 | Experiments

The devices of our experiment are illustrated in Figure 6. A droplet (radius: 1.25 ± 0.1 mm, containing gold nanoparticles) was dispensed from a needle positioned at a height of 3.0 ± 0.5 mm above the substrate. The droplets were deposited on a bar of brass (40 mm × 6 mm × 3 mm), which was precisely machined with an axial shallow parabolic groove (central depth 0.5 mm), serving to guide the droplet motion strictly along the x-axis. The bar was carefully leveled using a high-precision spirit level (accuracy: $\alpha_s \leq 0.1$ mrad) to ensure horizontal alignment.

The bar surface temperature was maintained at 310 ± 0.5°C to ensure the film boiling beneath the droplet, thereby preventing explosive boiling when the droplet contacts the substrate during detachment from the needle and subsequent directional motion. The bar surface temperatures were measured using two thermocouples positioned on the left and right sides, which are shown in Figure 6c. Each thermocouple was connected to a PID controller to adjust the heating power, maintaining the substrate surface temperature at 310 ± 0.5°C. Thus, the temperature deviation of the bar was controlled within 1.0°C to eliminate temperature gradients that could influence the thickness of the vapor film beneath the droplet, as shown in Figure S3. Additionally, the smooth surface of the substrate reduces unintended driving forces arising from asymmetric microstructures (see details in Figure S4).

Upon detachment from the needle, the droplet was immediately exposed to a pulsed laser with a spot diameter of 200 μm. The pulsed laser was emitted from an Nd: YLF laser device (PEGASUS PIV/XR) with a wavelength of 527 nm and a repetition rate of 200 Hz. The laser beam, focused by a convex lens with a focal length of 250 mm, was positioned at the center of the bar and at a height of 1.25 mm above the substrate. Leidenfrost droplets preferentially move along the bar's valley. Thus, the laser beam could always focus on the droplet's center from the left. The Rayleigh length $L_r = 0.25\pi d_1^2 / = 59.6$ mm was larger than the bar's length (40 mm) to maintain a stable laser energy density on the droplet. The single pulse energy E_l was adjustable between 0 and 8.0 mJ, whose stability was confirmed via an optical power meter (Figure S5). Droplet motion process was captured through two synchronized high-speed cameras: an overhead camera (Keyence W5000) operating at 2000 Hz with 61.4 μm/pixel resolution to track macroscopic motion, and a side-view camera (IDT, MotionPro Y4) running at 1000 Hz with 20.9 μm/pixel resolution to observe internal fluid behaviors of droplets with laser irradiation. Both cameras were synchronized with the pulsed laser via a high-precision timing controller, ensuring a synchronization error below 20 ns. Experiments were conducted at 22 ± 1°C and 30 ± 3% relative humidity to mitigate environmental influence.

4.2 | Materials

The 527 nm pulse laser was used in this study. And the deionized water exhibits weak absorption at this wavelength. Thus, the gold nanoparticles (AuNPs) were employed to enhance the light absorption. The gold nanofluid was prepared via the citrate reduction method. Gold(III) chloride hydrate ($HAuCl_4$, Au ≥ 49%) and trisodium citrate ($Na_3C_6H_5O_7$, 99.8%) were obtained from Sigma–Aldrich. An aqueous solution of $HAuCl_4$ was heated to boiling, followed by the addition of $Na_3C_6H_5O_7$, resulting in the formation of a wine-red gold nanofluid [29]. After ultrasonic treatment, the nanofluid exhibited enhanced stability, with no observable particle coalescence or sedimentation over an extended period. AuNPs were characterized by TEM (Hitachi S-5500) for morphology, as shown in Figure S6a. AuNPs with an average diameter of 19.47 nm, as determined by TEM, significantly enhance light absorption owing to localized surface plasmon resonance [40]. The hydrodynamic diameter of nanoparticles in solution was also characterized by dynamic light scattering (Malvern Zetasizer Nano ZS). Gold nanofluids have an average hydrodynamic diameter $d_{l,\,ave}$ of ~20.3 nm, which was slightly larger than the statistical value obtained from TEM. This was because the hydrodynamic diameter includes the citrate ions adsorbed on the AuNPs surface to stabilize the dispersion. The nanofluid concentration and whether it undergoes laser irradiation have minimal impact on the hydrodynamic diameter of the AuNPs, as shown in Figure S6c. This indicates that the high concentration and laser irradiation used in the experiment do not cause nanoparticle agglomeration. The surface tension coefficient of pure water was 70.53 mN/m, whereas that of the gold nanofluid at a concentration of 500 ppm was 69.54 mN/m. This small difference indicates that the presence of AuNPs has little effect on the surface tension of water.

16136829, 0, Downloaded from https://onlinelibrary.wiley.com/doi/10.1002/smll.202512574 by Jinliang Xu - North China Electric Power University Beijing , Wiley Online Library on [12/05/2026]. See the Terms and Conditions (https://onlinelibrary.wiley.com/terms-and-conditions) on Wiley Online Library for rules of use; OA articles are governed by the applicable Creative Commons License

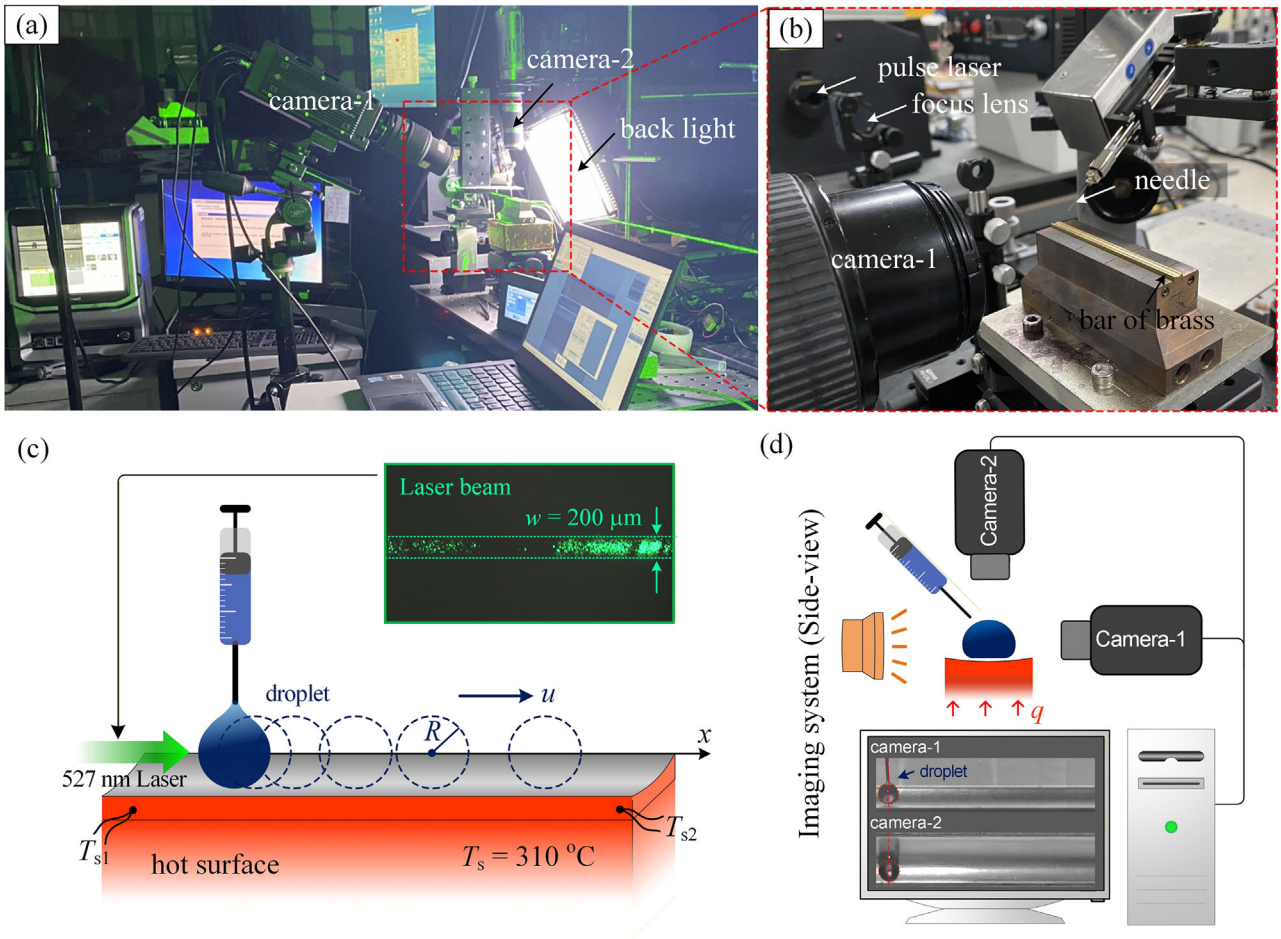


FIGURE 6 | The experiment setups. (a) Overview of the experimental system. (b) A magnified view of the experimental section. (c) Schematic diagram of the side view of the experimental setup. (d) Schematic diagram of the setup from the perspective of the laser device, illustrating the relative positioning of the two high-speed cameras. An overhead camera (Keyence W5000) operating at 2000 Hz with a resolution of 61.4 μm/pixel to track macroscopic motion, and a side-view camera (IDT, MotionPro Y4) operating at 1000 Hz with a resolution of 20.9 μm/pixel.

The detailed data are provided in Figure S6. The absorption performance increases with the nanofluid concentration. At c_i = 500 ppm, transmissivity at λ = 527 nm drops to 2.91% over a 2.5 mm path, which corresponds to the droplets' diameter. This optical modification was essential for investigating the impact of light absorption efficiency on the motion dynamics of Leidenfrost droplets under laser irradiation. For another laser wavelength, such as 1650 nm, the optical modification was not required, due to the high absorption of deionized water at this wavelength.

4.3 | Statistical Analysis

The experimental data were primarily obtained from images recorded by two high-speed cameras positioned for top and side views, respectively. Five independent experiments were conducted for each operating condition, and use this to calculate the experimental error. (1) The motion of Leidenfrost droplets was characterized using the top-view high-speed camera, as presented in Figure 1a. For the droplet in each image, four extreme points of the two-dimensional projected shape (top, bottom, left, and right) were identified, and the droplet center was determined from these points. This approach minimizes errors caused by droplet shape deformation during motion. Theoretically, the positional accuracy of this method was ± 61.4 μm, corresponding to the image resolution. Droplet motion parameters were obtained by tracking the temporal evolution of the droplet centroid positions. The data points in Figure 2a represent the displacement trends of droplet centroids under different operating conditions. By fitting these data, continuous motion curves were obtained, and the actual droplet accelerations a were calculated as the second time derivative of the fitted displacement, $a = d^2x/dt^2$. (2) The evolution of bubbles inside the droplet during motion was captured using a laterally positioned high-speed camera. Due to their small size, the bubbles inside the droplets were approximated as circles. The bubble centroid positions and sizes were then extracted from the images by identifying four extreme points of the fitted circles (top, bottom, left, and right). It should be noted that the bubble centroid positions obtained from the images do not represent their true locations due to refractive-index mismatches at the droplet–air interface. In this work, all image-derived positions were corrected to true values using the method described in the Supplementary Information. Bubble sizes were similarly affected by refraction and were corrected accordingly.

16136829, 0, Downloaded from https://onlinelibrary.wiley.com/doi/10.1002/smll.202512574 by Jinliang Xu - North China Electric Power University Beijing , Wiley Online Library on [12/05/2026]. See the Terms and Conditions (https://onlinelibrary.wiley.com/terms-and-conditions) on Wiley Online Library for rules of use; OA articles are governed by the applicable Creative Commons License

Acknowledgements

The authors acknowledge the support from the National Natural Science Foundation of China (52306195).

Conflicts of Interest

The authors declare no conflicts of interest.

Data Availability Statement

The data that support the findings of this study are available from the corresponding author upon reasonable request.

References

1. C. Kleinstreuer and Z. Zhang, "Airflow And Particle Transport In The Human Respiratory System," *Annual Review Of Fluid Mechanics* 42, no. 1 (2010): 301–334.

2. R. M. Bain, C. J. Pulliam, F. Thery, and R. G. Cooks, "Accelerated Chemical Reactions and Organic Synthesis in Leidenfrost Droplets," *Angewandte Chemie International Edition* 55, no. 35 (2016): 10478–10482, https://doi.org/10.1002/anie.201605899.

3. P. Agrawal, G. G. Wells, R. Ledesma-Aguilar, et al., "Leidenfrost Heat Engine: Sustained Rotation Of Levitating Rotors On Turbine-Inspired Substrates," *Applied Energy* 240 (2019): 399–408.

4. Z. Wu, L. Sun, H. Chen, and Y. Zhao, "Bioinspired Surfaces Derived From Acoustic Waves for On-Demand Droplet Manipulations," *Research* 6 (2023): 0263, https://doi.org/10.34133/research.0263.

5. X. Liang, V. Kumar, F. Ahmadi, and Y. Zhu, "Manipulation Of Droplets And Bubbles For Thermal Applications," *Droplet* 1, no. 2 (2022): 80–91, https://doi.org/10.1002/dro2.21.

6. L. Wang, K. Yin, Q. Deng, Q. Huang, J. He, and J. A. Duan, "Wetting Ridge-Guided Directional Water Self-Transport," *Advanced Science* 9, no. 34 (2022): 2204891.

7. M. Jiang, Y. Wang, and F. Liu, "Inhibiting The Leidenfrost Effect Above 1,000 °C For Sustained Thermal Cooling," *Nature* 601, no. 7894 (2022): 568–572, https://doi.org/10.1038/s41586-021-04307-3.

8. X. Zhao, S. C. Tan, C. Zhang, Y. Yao, and J. Liu, "Spinning Liquid Metal Droplets on Ice," *Small* 19, no. 29 (2023): 2300158.

9. I. U. Vakarelski, J. O. Marston, D. Y. C. Chan, and S. T. Thoroddsen, "Drag Reduction by Leidenfrost Vapor Layers," *Physical Review Letters* 106, no. 21 (2011): 214501, https://doi.org/10.1103/PhysRevLett.106.214501.

10. G. Graeber, K. Regulagadda, and P. Hodel, "Leidenfrost Droplet Trampolining," *Nature Communications* 12, no. 1 (2021): 1727, https://doi.org/10.1038/s41467-021-21981-z.

11. Y. Lin, F. Chu, Q. Ma, and X. Wu, "Gyroscopic Rotation Of Boiling Droplets," *Applied Physics Letters* 118, no. 22 (2021): 221601, https://doi.org/10.1063/5.0054248.

12. S. Lyu, V. Mathai, Y. Wang, et al., "Final Fate Of A Leidenfrost Droplet: Explosion Or Takeoff," *Science Advances* 5, no. 5 (2019): aav8081.

13. A. Bouillant, T. Mouterde, P. Bourrianne, A. Lagarde, C. Clanet, and D. Quéré, "Leidenfrost Wheels," *Nature Physics* 14, no. 12 (2018): 1188–1192, https://doi.org/10.1038/s41567-018-0275-9.

14. D. Quéré, "Leidenfrost Dynamics," *Annual Review of Fluid Mechanics* 45 (2013): 197–215.

15. S. Shi, C. Ma, S. Hardt, and C. Lv, "Leidenfrost Propulsion On Symmetric Textured Surfaces Via Spontaneous Symmetry Breaking," *Science Advances* 11, no. 17 (2025): adt6677, https://doi.org/10.1126/sciadv.adt6677.

16. R. Brandão and O. Schnitzer, "Spontaneous Dynamics Of Two-Dimensional Leidenfrost Wheels," *Physical Review Fluids* 5, no. 9 (2020): 091601, https://doi.org/10.1103/PhysRevFluids.5.091601.

17. H. Linke, B. J. Alemán, and L. D. Melling, "Self-Propelled Leidenfrost Droplets," *Physical Review Letters* 96, no. 15 (2006): 154502, https://doi.org/10.1103/PhysRevLett.96.154502.

18. G. Lagubeau, M. Le Merrer, C. Clanet, and D. Quéré, "Leidenfrost On A Ratchet," *Nature Physics* 7, no. 5 (2011): 395–398, https://doi.org/10.1038/nphys1925.

19. G. G. Wells, R. Ledesma-Aguilar, G. McHale, and K. Sefiane, "A Sublimation Heat Engine," *Nature Communications* 6, no. 1 (2015): 6390, https://doi.org/10.1038/ncomms7390.

20. K. Wang, H. Q. Zhang, Y. T. Wang, et al., "Power Generation From An Elastic Leidenfrost Hydrogel Piston Enabled Heat Engine," *International Journal of Heat and Mass Transfer* 179 (2021): 121661.

21. A. Bouillant, B. Lafoux, C. Clanet, and D. Quéré, "Thermophobic Leidenfrost," *Soft Matter* 17, no. 39 (2021): 8805–8809, https://doi.org/10.1039/D1SM00548K.

22. Q. Dai, M. M. Khonsari, C. Shen, W. Huang, and X. Wang, "Thermocapillary Migration of Liquid Droplets Induced by a Unidirectional Thermal Gradient," *Langmuir* 32, no. 30 (2016): 7485–7492, https://doi.org/10.1021/acs.langmuir.6b01614.

23. B. Sobac, A. Rednikov, S. Dorbolo, and P. Colinet, "Self-Propelled Leidenfrost Drops On A Thermal Gradient: A Theoretical Study," *Physics of Fluids* 29, no. 8 (2017): 082101, https://doi.org/10.1063/1.4990840.

24. F. Celestini and G. Kirstetter, "Effect Of An Electric Field On A Leidenfrost Droplet," *Soft Matter* 8, no. 22 (2012): 5992, https://doi.org/10.1039/c2sm25656h.

25. K. Piroird, C. Clanet, and D. Quéré, "Magnetic Control Of Leidenfrost Drops," *Physical Review E* 85, no. 5 (2012): 056311, https://doi.org/10.1103/PhysRevE.85.056311.

26. X. Sun, D. Kong, C. Liang, Y. Hu, and J. Duan, "Flexible And Precise Droplet Manipulation By A Laser-Induced Shape Temperature Field On A Lubricant-Infused Surface," *Langmuir* 38, no. 21 (2022): 6731–6740, https://doi.org/10.1021/acs.langmuir.2c00680.

27. Y. Yang, P. Jiang, and H. Li, "Photothermal-Driven Droplet Manipulation: A Perspective," *The Journal of Physical Chemistry Letters* 15, no. 34 (2024): 8877–8895, https://doi.org/10.1021/acs.jpclett.4c01977.

28. A. Biance, C. Clanet, and D. Quéré, "Leidenfrost Drops," *Physics of Fluids* 15, no. 6 (2003): 1632–1637, https://doi.org/10.1063/1.1572161.

29. X. Yan, J. Xu, Z. Meng, J. Xie, and H. Wang, "A New Mechanism of Light-Induced Bubble Growth to Propel Microbubble Piston Engine," *Small* 16, no. 29 (2020): 2001548, https://doi.org/10.1002/smll.202001548.

30. G. Liu, J. Xu, T. Chen, and K. Wang, "Progress In Thermoplasmonics For Solar Energy Applications," *Physics Reports* 981 (2022): 1–50, https://doi.org/10.1016/j.physrep.2022.07.002.

31. B. Sobac, A. Rednikov, S. Dorbolo, and P. Colinet, "Leidenfrost Effect: Accurate Drop Shape Modeling And Refined Scaling Laws," *Physical Review E* 90, no. 5 (2014): 053011, https://doi.org/10.1103/PhysRevE.90.053011.

32. H. Fu, X. Mei, and D. Yurchenko, "Rotational Energy Harvesting For Self-Powered Sensing," *Joule* 5, no. 5 (2021): 1074–1118, https://doi.org/10.1016/j.joule.2021.03.006.

33. H. Li, W. Fang, and Y. Li, "Spontaneous Droplets Gyrating Via Asymmetric Self-Splitting On Heterogeneous Surfaces," *Nature Communications* 10, no. 1 (2019): 950, https://doi.org/10.1038/s41467-019-08919-2.

34. D. J. You and J. Yoon, "Droplet Centrifugation, Droplet DNA Extraction, And Rapid Droplet Thermocycling For Simpler And Faster PCR Assay Using Wire-Guided Manipulations," *Journal of Biological Engineering* 6, no. 1 (2012): 15, https://doi.org/10.1186/1754-1611-6-15.

35. K. Sazawa, Y. Shanjana, K. Sugawara, and H. Kuramitz, "Rotating Droplet Hydrodynamic Electrochemistry for Water Toxicity Bioassay Based on Electron-Transfer Mediator," *Electrochem* 5, no. 3 (2024): 370–379, https://doi.org/10.3390/electrochem5030024.

16136829, 0, Downloaded from https://onlinelibrary.wiley.com/doi/10.1002/smll.202512574 by Jinliang Xu - North China Electric Power University Beijing , Wiley Online Library on [12/05/2026]. See the Terms and Conditions (https://onlinelibrary.wiley.com/terms-and-conditions) on Wiley Online Library for rules of use; OA articles are governed by the applicable Creative Commons License

36. C. Chen, Y. Gu, and J. Rufo, "Acoustofluidic Spin Control For 3D Particle Manipulation In Droplets," *Science Advances* 11, no. 20 (2025): adx0269, https://doi.org/10.1126/sciadv.adx0269.

37. K. Honda, K. Fujiwara, K. Hasegawa, A. Kaneko, and Y. Abe, "Coalescence And Mixing Dynamics Of Droplets In Acoustic Levitation By Selective Colour Imaging And Measurement," *Scientific Reports* 13, no. 1 (2023): 19590, https://doi.org/10.1038/s41598-023-46008-z.

38. L. Garibyan and N. Avashia, "Polymerase Chain Reaction," *Journal of Investigative Dermatology* 133, no. 3 (2013): 1–4, https://doi.org/10.1038/jid.2013.1.

39. D. M. Katschinski, "On Heat And Cells And Proteins," *Physiology* 19, no. 1 (2004): 11–15, https://doi.org/10.1152/nips.01403.2002.

40. C. Kuppe, K. R. Rusimova, L. Ohnoutek, D. Slavov, and V. K. Valev, ""Hot" in Plasmonics: Temperature-Related Concepts and Applications of Metal Nanostructures," *Advanced Optical Materials* 8, no. 1 (2020): 1901166, https://doi.org/10.1002/adom.201901166.

Supporting Information

Additional supporting information can be found online in the Supporting Information section.

Supporting File 1: smll73767-sup-0001-SuppMat.docx.

Supporting File 2: smll73767-sup-0002-MovieS1.mp4.

Supporting File 3: smll73767-sup-0003-MovieS2.mp4.

16136829, 0, Downloaded from https://onlinelibrary.wiley.com/doi/10.1002/smll.202512574 by Jinliang Xu - North China Electric Power University Beijing , Wiley Online Library on [12/05/2026]. See the Terms and Conditions (https://onlinelibrary.wiley.com/terms-and-conditions) on Wiley Online Library for rules of use; OA articles are governed by the applicable Creative Commons License